Modeling the Kinetic and Thermal Interaction of UWS Droplets Impinging on a Flat Plate at Different Exhaust Gas Conditions

Antonello Nappi, Gianluca Montenegro, Angelo Onorati, and Augusto Della Torre Politecnico di Milano

Panayotis Dimopoulos Eggenschwiler Empa

Abstract

The selective catalytic reduction has seen widespread adoption as the best technology to reduce the NO_x emissions from internal combustion engines, particularly for Diesels. This technology uses ammonia as a reducing agent, which is obtained injecting an ammonia carrier into the exhaust gas stream. The dosing of the ammonia carrier, usually AdBlue, is the major concern during the design and engine calibration phases, since the interaction between the injected liquid and the components of the exhaust system can lead to the undesired formation of solid deposits. To avoid this, the thermal and kinematic interaction between the spray and the components of the after treatment system (ATS) must be modeled accurately. In this work, the authors developed a Conjugate Heat Transfer (CHT) framework to model the kinetic and thermal interaction among the spray, the eventual liquid layer and the pipe walls. The Nukiyama curve has been embedded in the calculation of the heat flux between the droplet and the walls to limit the heat transfer in the proximity of the Leidenfrost point and in the transition region. To validate this model, an experimental data set was provided by EMPA (CH) and used for comparison with calculated values. The measurement of the thermal footprint of the spray have been performed on the back of a thin plate where the spray impinges. Several injections have been considered with the intent of showing the transition to the different interaction regimes. The simulations performed show that after the initial cooling of the wall, due to impingement, a liquid film is formed, which is then dragged along the plate. As the number of injection progresses, the effect of the transition between the different evaporation regimes translates into high temperature gradients on the back of the plate. The comparison with the experimental data both in terms of temperature and temperature gradient shows a good agreement with the experiments, showing the capabilities of the model developed to predict the temperature drop.

Introduction

The increasing restrictions on vehicle emissions in these years have spurred the development and application of efficient exhaust after treatment technologies [1]. For Diesel internal combustion engines this entails a reduction of particulate matter (PM) and nitric oxides (NO). Selective Catalytic Reduction (SCR) has confirmed in these years its role as a cost effective and efficient way to control the emissions of NO. The reduction of NO in these systems is performed through the use of a reducing agent, in the form of ammonia, which is introduced in the exhaust gas flow as a diluted (32.5 % wt) Urea Water Solution, also known as Diesel Exhaust Fluid (DEF) or AdBlue. The urea water solution (UWS) injected is heated by the exhaust gases and undergoes an hydrolysis and thermolysis process [2], leading to the release of gaseous ammonia. To ensure the maximum efficiency of conversion, the ammonia formed must be distributed as uniformly as possible in the exhaust gases before the entry to the catalyst itself. To do so, a mixer is usually placed before the catalyst entrance [3]. The highly transient condition

of the exhaust system, coupled with the limited space available for the after-treatment system, makes the complete evaporation of the spray a challenging task. In particular, the interaction between the spray and the mixer is mostly unavoidable and will have an important role in enhancing the heat transfer to the spray and in improving the evaporation by breaking up the droplets with large diameter. This strong thermal interaction can rapidly lead to local cooling of the wall [4], with consequent formation of liquid film, once the wetting threshold is reached. When the liquid film forms, depending on the temperature and residence time, byproducts of the decomposition of the urea in the film can lead to the formation of solid deposits. These byproducts include biuret, cyanuric acid, ammelide and triuret [5]. These form more permanent deposits, that by progressive accumulation can lead to a serious reduction in the system efficiency, by reducing the availability of ammonia at the catalyst and altering the flow pattern in the area of the deposit formation. As the formation of liquid film is in any case the precursor to the development of solid deposits [6], an accurate prediction of

the film dynamics is necessary, both from a kinematic and thermal point of view. Since the competition between the evaporation of the film and the conversion of the film itself onto deposits is what ultimately controls the fate of the film, an accurate modeling of the chemistry and heat exchange between the solid and the film is needed. For the modeling of the heat transfer different models have been proposed, such as the one proposed by Birkhold [7], that takes into account the effect of surface overheat on the heat flux between film and solid surfaces (Leidenfrost effect). Regarding the chemistry of urea decomposition, numerous studies are available [8, 9, 5]. To ascertain the characteristic temperatures of the chemical reactions for each specie a thermogravimetric analysis is used. However [9] has highlighted the dependence of this technique on the crucible geometry adopted. The effect of the different chemical properties of urea and water and in particular the strong difference in vapour pressure between the two chemical species is apparent in the characteristic three stage evaporation of UWS [10]. Namely, after the droplet heats up, the water, being the specie with the higher vapour pressure evaporates from the droplet. After the evaporation of water, the thermolysis of urea into ammonia and isocyanic acid starts, followed by the gaseous reactions, mostly the hydrolysis of isocyanic acid into ammonia and carbon dioxide. Due to the complexity of the process, different authors [11, 12] have developed reduced models, with different strategies to model the evaporation and decomposition process. To correctly predict the transition from non-wetting to wetting regime, a correct evaluation of the heat flux between the spray and the ATS components is necessary. For temperatures above the wetting threshold, Wruck [13] postulated that droplets impinging on dry wall experience a strong heat flux, much higher than the one possible once a vapour blanket is established on the surface. The evaluation of the heat flux in this regime can prove to be extremely difficult, with most studies involving droplets in We ranges far from the ones seen in the ATS [14]. The effects of the kinematic interaction between spray and wall have been described by different models, such as the one proposed by Bai and Gosman [15, 16], and adapted to the injection of UWS [17]. The complexity of the models involved is coupled to the vastly different time scales of the different phenomena that needs to be modeled, spanning from the millisecond time scale of the injection process to the minutes necessary for the formation of solid deposits. In this article, the authors have implemented the Kuhnke [18] model (which will be described later) in the open source software OpenFOAM along with a fully coupled Conjugate Heat Transfer (CHT) model [19] capable of modeling the heat transfer between spray and solid domain, as well as between film and solid and bulk gas and solid. Finally, a heat transfer model for the liquid film is implemented, considering the change in heat flux in the different boiling regimes. To have a meaningful comparison, the authors have performed first a tuning of the spray model ensuring that the film formed in wetting conditions has a similar extension to the one produced experimentally in the same conditions. This model is then applied to a test case with multiple injections [4], showing the capabilities of the model to capture the transition from dry to wet spray wall interaction and to fully capture the temperature transient.

Spray/Wall Model Interaction Description

The interaction between spray and wall is a very complex phenomenon, influenced by many parameters, such as the parcel velocity, the wall roughness and temperature [20]. Several models were developed to reproduce the effects of this interaction. The model chosen is the one proposed by Kuhnke [18]. In this model, the range of possible interactions is reduced to four different possible regimes: deposition, splash, rebound and thermal breakup. The classification is based on the definition of two parameters:

1. The thermal parameter T^*, which captures the temperature dependence, and is defined as the ratio between the wall temperature and the fluid saturation temperature $\dfrac{T_w}{T_{sat}}$.
2. The Kinematic parameter K, which takes into account the effect of inertia, surface tension and viscous forces, and can be written as the ratio of Weber and Laplace number $We^{\frac{5}{8}} La^{\frac{1}{8}}$

With these two parameters, the different impingement regimes can be represented on a map, reported in Figure 1.

The four different impingement regimes can be distinguished by considering a T^* threshold value (T^*_{crit}) that represents the deposition limit for the droplets, and two different critical K values (K_{crit}), one for dry and one for wet conditions ($K_{crit, hot}$ and $K_{crit, cold}$ respectively). The value of T^*_{crit} is still debated, with values ranging from 1.25 to 1.43-1.47 [7] depending on the specific application. In particular, the values taken from Birkhold [7] assumes that the wetting threshold coincides with the Leidenfrost temperature, assumption that is used also in this paper. Above this temperature, the formation of a vapour layer prevents the contact between the droplets and the wall, leading to the reflection of impinging droplets, with and interaction that could be either destructive (thermal breakup) or non-destructive (rebound). When the wall temperature is below the critical temperature, the droplets instead form a liquid layer on the wall. In the splashing regime, this is accompanied by the atomization of part of the droplet

FIGURE 1 T^*-K diagram, with different impact regimes.
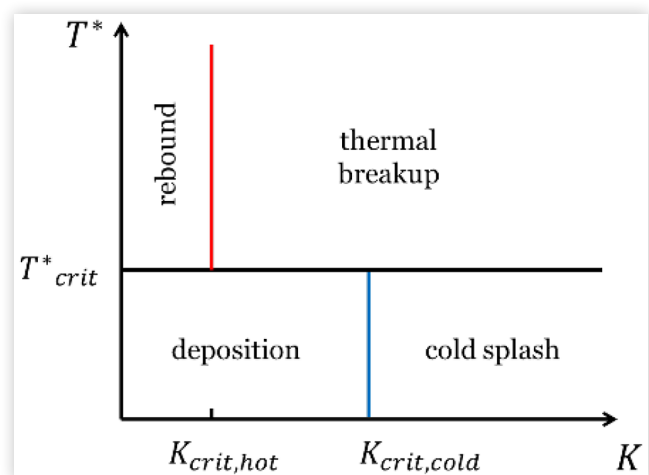
and formation of secondary droplets (similarly to the thermal breakup interaction). If the value of K is below the critical value, the droplets will form a surface film layer.

Since no clear effect of the impingement angle is proposed in the literature, the evaluation of the K parameter is based on the formulation of a normal We number We_n, considering only the normal component of the velocity. Regarding the critical values K_{crit}, two different formulations are used for dry and deposition conditions. For dry condition, due to the limited interaction between the droplet and the wall (because of the vapour layer) $K_{crit, hot}$ is defined by Kuhnke [18] as a uniform probability function with value between 20 and 40. Below T^*_{crit}, the direct interaction between wall and droplets lead to a more complex formulation for $K_{crit, cold}$, depending on T^* and wall roughness. In this case the $K_{crit, cold}$ decreases with an increase in temperature [18] (reaching a minimum when the temperature reaches the critical T), as the boiling of the droplet increases the probability of destructive interactions, and with roughness [20], as rougher surfaces will induce more destructive interactions. As the temperature increases, the formation of vapour reduces the interaction between droplets and wall crevices, reducing the effect of wall roughness. To determine the outcome of the interaction, different properties must be evaluated, such as the mass fraction off the secondary droplets, size ratio, velocity magnitude and direction, and number of parcels required to fulfill the mass balance.

The mass ratio, which describes the mass of the parcel after the interaction, was determined using a semi empirical function from [15], corrected to take into account the transition to hot wall impingement and interaction with surface film. Two formulations are used, depending on the presence/absence of liquid deposition, determined from the value of T^* (with the Leidenfrost temperature as threshold). The value of the mass ratio can assume values above one, representing the case when impingement on film removes mass from the film itself.

Regarding the size ratio, two formulations are used, again depending on the deposition condition. For dry wall, the formulation by Kuhnke [18] is used, while for wet conditions the one from Nagaoka [21] was adopted. In the case of a rebound interaction the diameter of the parcel is assumed to remain unchanged. The velocity of the secondary droplets was assumed to depend only on the nature of the interaction (breakup or rebound). For simple rebound cases, the velocity is determined by imposing the conservation of momentum in the tangential direction and a reduction of the normal component of velocity. The normal component of the velocity is evaluated from the We number of the parcel after the interaction, which is calculated using a formulation from [22]. In the case of destructive interactions, two different formulations [21] are used depending on the deposition condition. The ejection angle needs to be determined only in cases when the interaction is destructive, as for rebound cases it is dictated by the conservation of tangential momentum and the evaluation of the new normal velocity. For destructive interactions, again a distinction between cases above and below deposition limit is done: when the temperature is below the deposition limit, the ejection angle was found to be dependent on the droplet incidence angle and on the wall roughness, while for temperatures above the wetting threshold Mundo [20], and Nagaoka [21] found a dependence on the Weber number. The value of the ejection angle is evaluated

starting from a mean value which is determined depending on the impingement conditions (wet or dry, cold or hot) and then using a logistic distribution with an assigned scale parameter to determine the value which is later assigned to the ejected parcel. For the deviation angle, a further distinction must be done, as in the case of orthogonal impingement the direction is selected in a random planar direction. For angle below 90 degrees, the distribution is condensed at the leeward side, and diluted in the windward direction. This condition reflects the conservation in tangential momentum, and the deviation angle (ψ) is found using a formula from [18]. Once all the kinematic quantities of the parcel have been found, the computation of the number of parcels to generate after the interaction is found from the conservation of mass and the size ratio. Kuhnke [18] proposes to generate three parcels after each destructive impact, with average diameter for the parcels evaluated from a Weibull distribution.

Thermal Modeling

During the interaction, the heat exchange between wall and parcels is evaluated using a semi-infinite body approach, as proposed by Wruck [13]:

$$Q = A_{con} \frac{2\sqrt{t_{con}}}{\sqrt{\pi}} \frac{b_w b_p}{b_w + b_p} (T_w - T). \tag{1}$$

The energy exchanged depends on different quantities, such as the effusivities of the parcel and of the wall (b_p, b_w), evaluated as:

$$b = \sqrt{\rho \lambda c_p}. \tag{2}$$

As well as on other parameters depending on the type of interaction, such as the contact time (t_{con}), the contact area (A_{con}) and temperature difference. The contact time is a function of the K parameter of the impinging droplet, with two formulas used depending on the value of K. The threshold value used ($K = 40$) corresponds to the threshold between rebound and thermal breakup interactions:

$$t_{con} = \begin{cases} \sqrt{\dfrac{\pi}{2} \left(\dfrac{pD^5}{\sigma U^2} \right)^{0.25}} & \text{for } K \leq 40 \\[4ex] \dfrac{\pi}{4} \sqrt{\dfrac{pD^3}{\sigma}} & \text{for } K > 40 \end{cases} \tag{3}$$

FIGURE 2 Schematic of the different angles used in the model with: α: impingement angle, β: ejection angle, ψ: deviation angle.
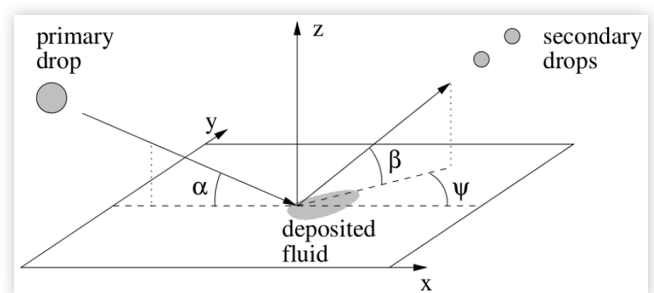
During contact, the droplet deforms as the inertia forces are converted into surface tension forces, and this is reflected in the evaluation of the contact area, which is assumed to have a triangular profile, with the maximum contact area evaluated starting from the maximum spread diameter taken from Akao [23]:

$$D_{con,max} = D0.61We^{0.38}. \tag{4}$$

During the interaction, the parcel properties are updated, taking into account the heat flux from the wall and the interaction with the gaseous phase (mainly evaporation of the most volatile specie). This model does not consider the effect of the surface temperature on the heat transfer coefficient. To take into account this effect, the heat calculated from the Wruck model (equation 1) is used at each time step to evaluate an equivalent heat transfer coefficient (HTC), where ΔT and δ_{time} represent the temperature difference between wall and parcel and the time step length, respectively:

$$HTC_{parcel} = \frac{Q}{A_{con}\Delta T \delta_{time}}. \tag{5}$$

This heat transfer coefficient is then compared with the one obtained from the Nukiyama curve for that temperature at the specified wall temperature. If the heat transfer coefficient is above the one evaluated from the Nukiyama curve, the value is limited to that one and is then used to compute the energy to be transferred to the wall. The limiting function used is derived from the model developed to limit the heat transfer coefficient between the film and solid region, and the evaluation of the heat transfer coefficient will be explained in the following sections.

Liquid Film Modeling

The simulation of the liquid film is performed in OpenFOAM by defining a single layer region on the surfaces where formation of film is expected, and solving the associated conservation equations (mass, momentum, energy and species). The formulations of the conservation equations is done under this set of assumptions:

- The film is considered thin enough to apply a boundary layer approximation, meaning that the spatial gradients in tangential direction are much smaller than the ones in normal direction;

- The motion of the film is caused by tangential gradients of the total pressure, shear stresses at the wall and bulk gas interfaces, momentum sources from the impinging droplets and body forces;

- The local liquid pressure p_L can be considered constant across the depth of the film;

- The pressure p_L in the liquid depends on the following terms: the pressure of the gas p_g, pressure due to droplet impingement p_d, hydrostatic pressure p_h and capillary pressure p_σ Thus, locally if can be written as:

$$p_L = p_g + p_d + p_\sigma + p_h. \tag{6}$$

- The mass source term from the impingement of droplets can be considered a continuously differentiable function.

The coupling between the film and the spray, bulk gas and solid walls is achieved through the introduction of source terms in the appropriate conservation equations. The formulation of these equations will be now discussed, starting from the continuity equation.

Continuity Equation The continuity equation, under the previously stated assumptions, with the further assumption of incompressible flow can be written as a function of the film thickness h:

$$\frac{\partial h}{\partial t} + \nabla \cdot \left(h\vec{U}_f\right) = S_M + S_V. \tag{7}$$

The terms on the right-hand side of equation (7) represent respectively the source term due to droplet impingement (S_M) and the term due to evaporation (S_V) [24]. The first term can be written as:

$$S_M = \frac{4\pi\rho_d}{3A\rho_f \Delta t} \sum_{i=1}^{N_d} r_i^3. \tag{8}$$

where r_i is the radius of the ith parcel absorbed and ρ is the density. The prefix f refers to film properties, while d refers to droplet properties. The term due to evaporation is decomposed in two further terms $S_{v,k}$ and $S_{m,k}$. The first term takes into account the evaporation due to mass transport (prevailing for high flow stream velocities), and can be expressed as:

$$S_{V,k} = \frac{\left|\vec{\tau}_g\right|}{\rho_f \left|\vec{u}_\infty - \vec{u}_s\right|}\left(\left(B_k + 1\right)^{1/Sc_k} - 1\right); \tag{9}$$

While the second term takes into account the thermal effects (prevailing at high gas temperatures). This second term will be dominant for parcels evaporating in contact with the wall, due to the high heat fluxes combined with low gas velocities.

$$S_{V,k} = \frac{j_s}{\rho_f c_P \left(T_\infty - T_s\right)}\left(\left(B_k + 1\right)^{1/Le_k} - 1\right). \tag{10}$$

In both equations (9) and (10) the term ∞ refer to the properties of the bulk gas, while the quantities indicated with the subscript s refer to the quantities on the film surface (evaluated using the one third rule instead of the arithmetic average between cell center and gas). Le in the equation (10) refers to the Lewis number (ratio of thermal diffusivity to molecular diffusivity). When multiple species are present in the droplet, as is the case for UWS, the evaporation rates for each species are evaluated, and the overall evaporation rate is finally calculated as the sum of the individual species evaporation rates multiplied by the species mass fraction.

Species Equation The presence of multiple species in the film requires the solution of an additional set of $N_s - 1$ conservation equations (where N_s is the number of chemical species).

$$\frac{\partial hY_{f,k}}{\partial t} + \nabla \cdot \left(h\vec{U}_f Y_{f,k}\right) = S_{M,k} + S_{V,k}. \tag{11}$$

The equation is solved for the mass fraction of each specie, where the two source terms on the right-hand side correspond to the source terms seen for the continuity equation, on a per-specie basis.

Momentum Equation The liquid film momentum equation can be similarly formulated:

$$\frac{\partial h\vec{U}_f}{\partial t} + \nabla \cdot \left(h\vec{U}_f\vec{U}_f \right) = -\frac{1}{\rho_f}\nabla\left(hp_l \right) + \vec{\tau}_{fs} - \vec{\tau}_w + h\vec{g}_t + \vec{S}_U. \quad (12)$$

On the right-hand side of this equation several source terms can be found, representing the different causes of film motion. $\vec{\tau}_{fs}$ and $\vec{\tau}_w$ represent the viscous forces, at the gas and wall interface, g_t is the tangential component of the gravitational force, ∇p_l represent the term due to the gradient in pressure, while S_U is the tangential component of the source term due to droplet impingement. This term is particularly important in the primary impingement zone of the spray, whenever the axis of the injector is not perpendicular to the impingement surface, or there is strong spray/gas interaction, and can be written as:

$$\vec{S}_U = \frac{4\pi\rho_d}{3A\rho_f\Delta t}\sum_{i=1}^{N_d} r_i^3 \left(\vec{u}_i \cdot \underline{t} \right)\underline{t}. \quad (13)$$

The normal component of this term gives rise to a pressure term in the gas phase.

Energy Equation The energy equation for the film must take into account the effects of the thermal interaction with gas, spray and solid boundaries.

$$\frac{\partial hH_{s,f}}{\partial t} + \nabla \cdot \left(h\vec{u}_f H_{s,f} \right) = j_g - j_w + S_H, \quad (14)$$

In turn, these are represented in the equation by the source terms S_H, j_g and j_w. The term S_H represents the sensible enthalpy contribution:

$$S_H = \frac{4\pi\rho_d}{3A\rho_f\Delta t}\sum_{i=1}^{N_d} r_i^3 \hat{H}_{d,i}, \quad (15)$$

where $H_{d,i}$ is the sensible enthalpy of the impinging droplet.

Regarding the heat flux from the gas (j_g), this term is evaluated from the temperature gradient across the interface and takes also into account the heat flux due to evaporation.

Finally, the term j_w takes into account the effect of the heat flux from the wall, and it is evaluated using the heat transfer coefficient calculated by the model and the temperature gradient. As this term can be dominant, utmost care must be taken when evaluating it. This term is dependent on the temperature gradient between film and wall and the heat transfer coefficient between the two. The model that is used to evaluate this heat transfer coefficient will be discussed in the next chapter.

Heat Transfer Coefficient Model The evaluation of heat transfer coefficient at different solid temperatures is fundamental to appraise the correct evolution of the temperature of any surface where film formation occurs. In particular, for areas where the film forms and persists, the heat transfer between film and solid becomes the main source of cooling and represents the most dangerous conditions for solid deposit formation.

The model developed was based on the one proposed by [7], and is based on the Nukiyama curve of pure water (since there is an absence of data on the Nukiyama curve for UWS). Depending on the excess temperature (ΔT_e), defined as the difference between the wall temperature and the saturation temperature of the fluid, the different boiling regimes are identified [25]. During the evaluation of the heat flux to apply to the solid region (which is considered only when the film reaches a threshold height, to avoid numerical instabilities), the solid/film heat transfer model activates, and the model uses the information on the excess temperature to evaluate the heat flux and then the heat transfer coefficient.

FIGURE 3 The test case geometry: (a) Experimental temperature gradient as function of the average back plate temperature for different conditions investigated in [4] (b) Nukiyama boiling curve for water, taken from [25].

(a)

(b)
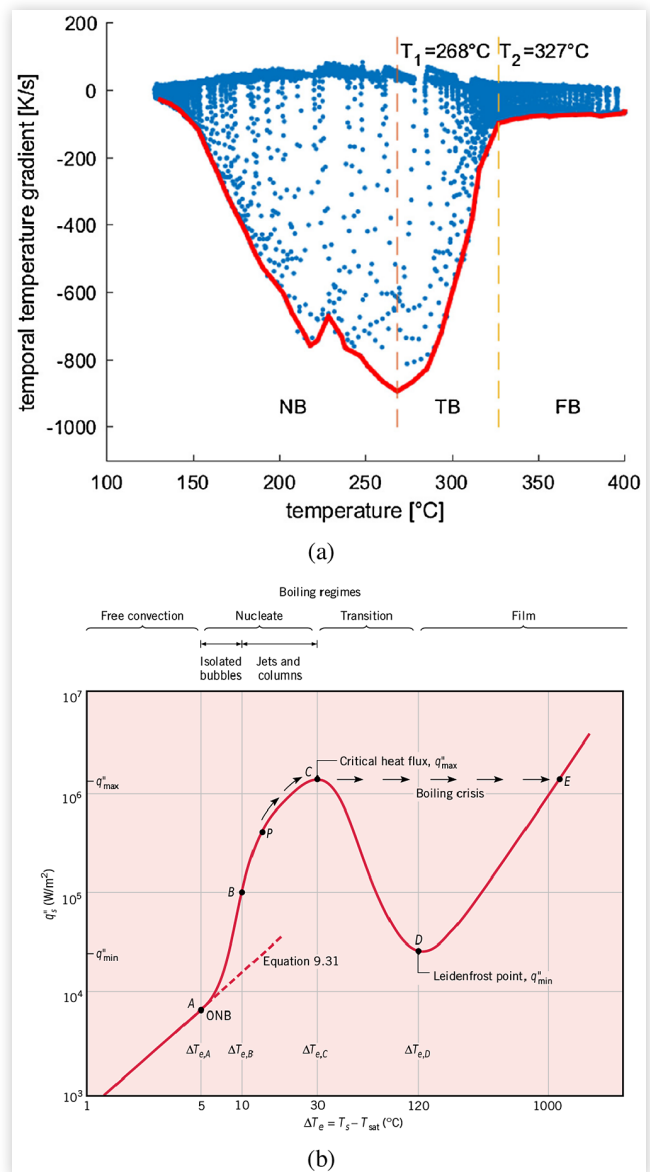
Since the heat transfer coefficient varies strongly between the different interaction regimes, it is important to use the correct values of excess temperature to delimit the different boiling regimes. In Figure 3, a graph of the temperature gradient as function of the temperature of the back side of the plate is reported above the Nukiyama curve for water. The parallels between the two graphs are apparent, as for the highest temperature (marked by FB in the graph) the temperature gradient shows a plateau, corresponding in the Nukiyama curve to the region near the Leidenfrost point. Afterward, in the transition boiling regime the increase in temperature gradients is reflected in the Nukiyama curve by the increase in heat fluxes characteristic of the transition regime. At the end of the transition boiling regime, the critical heat flux is reached, at a temperature of 268° C. From this point on, the nucleation boiling regime shows a reduction of the temperature gradients, again mirroring the behaviour of the Nukiyama curve, which shows a monotonous reduction in the heat fluxes. In this case, the availability of data on the temperature gradients measured at different plate temperature were used to deduce the critical heat flux temperature and the Nukiyama temperature. In Figure 3, the wall temperatures used as threshold for the Critical Heat Flux and the Nukiyama temperature are also highlighted. As these values refer to measurements taken on the back side of a target plate, they cannot be used as is and need to be converted to the corresponding temperature on the impingement side of the plate. To convert these values to the corresponding temperature values for the front of the plate, the analysis performed in [4] regarding the inverse heat transfer problem was utilised. Since the model employs the values of excess temperature to delimit the different evaporation regimes, these values then need to be converted to excess temperatures, requiring an estimate of the saturation temperature of the UWS at impingement conditions. This temperature was evaluated from the data available from previous simulations carried out on the same case, by averaging the saturation temperatures of the parcels interacting with the wall during one injection. These data allowed us to evaluate the CHF and Nukiyama temperature at 170 K and 65 K respectively. Both values differ considerably from the ones utilised for water (respectively 120 and 30 K). The value for the Nukiyama temperature was also utilised to evaluate the value of T_{crit}^*, leading to a value of 1.42, close to the value found in [7].

The details of the model will be now discussed, focusing on the different method used to evaluate the HTC for each evaporation regime. As the Nukiyama curve provides heat fluxes for the different excess temperatures, these values of the heat flux must be converted to heat transfer coefficients using the temperature difference between the wall and the interacting media (parcel or film). In particular, for the free convection regime ($\Delta T_e < 5$), the value of the heat flux is evaluated as the linear interpolation between the value calculated for pure conduction (eq. 16) and the minimum heat flux coefficient for the Nucleate Boiling regime:

$$Q_{f-w} = \frac{2\dfrac{\lambda_f}{h_f}\dfrac{\lambda_w}{h_w}}{\dfrac{\lambda_f}{h_f} + \dfrac{\lambda_w}{h_w}}\Delta T_e, \qquad (16)$$

TABLE 1 HTC model: tuning parameters for the different evaporation regimes.

f_0	1.4
f_1	1.4
f_2	25

where ΔT_e is the excess temperature, λ is the thermal conductivity, h is the plate thickness, and the suffix f and w refer to film and wall quantities, respectively.

In the nucleate boiling regime, ($5 < \Delta T_e < 65$) values of the heat flux are retrieved from a sigmoid interpolation of the heat flux constructed from data relative to water. This curve was manipulated to fit the new values for the CHF, since, as discussed before, this temperature does not correspond with the one of water. For the transition boiling regime ($65 < \Delta T_e < 170$) heat flux is evaluated as linear interpolation between the maximum value of heat flux for the nucleate boiling regime and minimum heat flux at the Leidenfrost temperature. The value of the minimum heat flux is evaluated using the formula derived by Zuber [26]:

$$Q_{min} = C\rho_v h_{fg}\left[\frac{g\sigma(\rho_l - \rho_v)}{(\rho_l + \rho_v)^2}\right]^{1/4} \qquad (17)$$

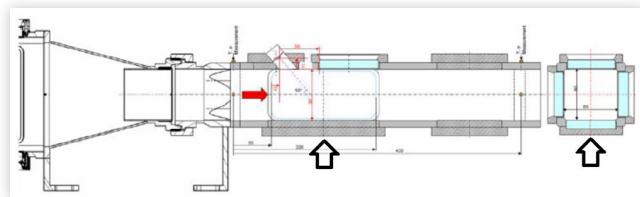where C = 0.09 in the case of flat plates.

For all evaporation regimes the heat flux is then converted to an HTC using the film/wall temperature difference as previously described. The value of the heat transfer coefficient is then used by the solver to evaluate the heat flux between the two regions, which is used as a source term for the energy equations of the liquid film and of the solid region. During the development, a need for some tuning of the HTC obtained from the Nukiyama curve arose and the authors applied different tuning parameters for the 3 different evaporation regimes. These parameters are referred to as f_0, f_1 and f_2, respectively for the free convection boiling, nucleate boiling and film boiling regimes. The values of these parameters are reported in the Table 1.

As it can be seen, while the values for the convective and nucleate boiling regimes are quite close to 1, the value for the film boiling regime is larger, reflecting the higher uncertainty behind the Zuber formula [25].

Validation Test Case

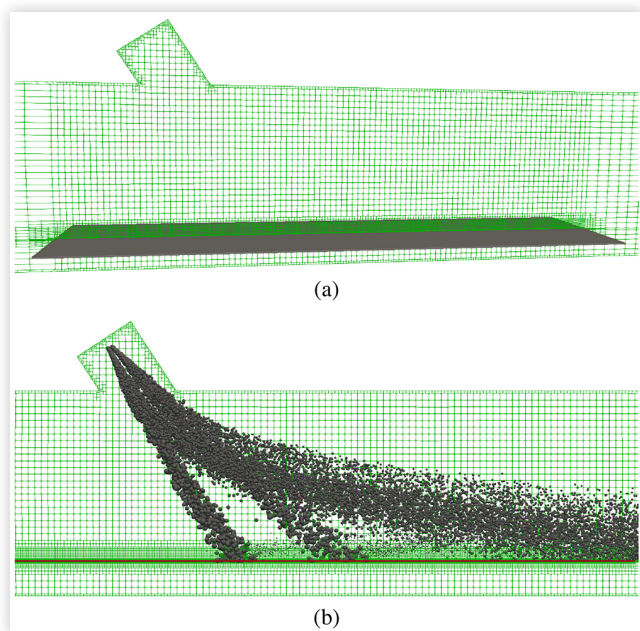To test the model, a case from Empa [4] was selected, due to the wide range in solid temperatures involved during the test, that will allow us to look at the behaviour of the model for different solid temperature, starting from dry conditions reaching wetting temperatures. The Empa test bench (see Figure 4) is designed with the objective of investigating conditions similar to the one present in the exhaust of diesel internal combustion engine, allowing a more realistic analysis of the evolution of UWS spray in such environment. Both the temperature and mass flow rate of the gases can be controlled independently. This is achieved using as air source the compressed air from the EMPA pressurized air network and controlling the mass flow rate through an anemometer. The

FIGURE 4 Schematic diagram of the EMPA test rig. The quartz window used for thermal imaging is indicated with a black arrow.

TABLE 2 Empa case: BC and injector data.

Inlet M	100 kg/h
Inlet U_{avg}	8.28 m/s
Inlet T	673 K
n Holes	3
Hole D	190 μm
Diameter @ hole center	1.9 mm
Inj P	9 bar
Mass per injection	0.2 g
Injection frequency	2 Hz
Injection duration	100 ms

temperature of the gases is controlled using three heating units, thus ensuring total independence of mass flow rate and temperature control, which is difficult to achieve when using an internal combustion engine as gas source. Once the gases reach the target temperature, they are fed to a testing section, where a UWS dosing unit injector is mounted, that is equipped with multiple windows, allowing optical access to perform analysis on the spray. Furthermore, a plate target is used to evaluate film formation and evolution during multiple injections, as well as monitoring the formation of solid deposits. This section has an 80 by 80 mm internal cross section, and in the cases analyzed, a thin (0.7 mm) stainless steel plate is positioned at 14 mm from the bottom of the tunnel. The temperature on the back side of the plate is evaluated by infrared thermometry, using one of the windows access available below the plate together with a 45-degree gold-plated mirror. To perform the thermography, a high speed camera was used, with a frame resolution of 640x512 pixels, and a frequency of 200 Hz [4]. Simulations were carried out considering just a fraction of the overall Empa test bench, in particular only the test chamber was modeled, and the resulting mesh is shown in Figure 5, with two details showing the recess

FIGURE 5 The test case geometry: (a) Side view of the fluid mesh, with solid mesh in grey. (b) Detail of the mesh, with a visualization of the spray during injection.

(a)

(b)

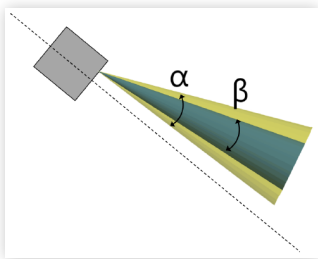where the injector is located and the metal plate used as spray target. To reduce the number of elements, the regions before and after the plate target which do not influence the spray wall interaction were meshed increasing the mesh dimension in the flow wise direction. The UWS was injected using a 3 hole injector, whose characteristics are reported in Table 2. The injector used has been previously characterised both in term of the diameter distribution [27] using phase doppler anemometry, but at a lower temperature (300 C). For the same injector a mass distribution analysis was performed, using a mechanical patternator to evaluate the mass distribution for each hole [28]. The boundary conditions in term of mass flow rate of gases and temperature are reported in Table 2.

The calculation grid was created targeting the best compromise between numerical accuracy and cell count. Since the evaluation of the solid temperature is required, a multi-region approach to the mesh generation is used. This leads to the generation of a conformal interface, needed to ensure the communication between the different regions involved in the simulation. The mesh in the solid region is refined in the direction of the thickness, to ensure a correct reconstruction of the temperature gradient inside the solid, which is crucial for the correct evaluation of the heat exchange, as the surface temperature is used to evaluate the heat flux to the plate itself. Since the liquid film is solved with a boundary layer approximation, the generation of a single layer mesh is necessary. This mesh was obtained as an extrusion from the previously defined solid/fluid interface, thus ensuring a correct face to face addressing when communicating between this region and the fluid region.

The simulation was set up using first order schemes for both liquid film and fluid domains, and the turbulence model used is the $k - \omega$ SST model. For the solution of the liquid film also first order schemes were used. The spray was modeled using a lagrangian phase, with spherical drag and gravity forces applied, heat transfer modeled using the Ranz Marshall model and with phase change activated. At the interaction with the walls, the Kuhnke model was used to predict the behavior of the parcel. To reproduce the cone shape, for each hole two different cone regions were defined, one reproducing the external part of the spray cone and the other reproducing the spray core. A simplified schematic of this process is shown in Figure 6, where the full cone (defined by the angle α) is split in a central full cone (with angle β) and an external hollow cone, representing the external part of the spray. This splitting is used to better capture the non-uniform distribution of mass

FIGURE 6 Visualisation of the cone splitting method used to reproduce the spray of every injector's hole. The dashed line represents the axis of the injector.

FIGURE 7 Visual comparison of the numerical and experimental film footprint, A and B are the transveral maximum semi extensions: A = 9.06 mm, B = 9.82 mm

flux due to the presence of ligaments and high diameter droplets in the center of the cone. For simplicity's sake, Figure 6 reports this concept only for one injector hole, but it has been applied to every single holes of the injector. The diameter distributions and mass fluxes for both cones were obtained starting from the original full spray distribution by manually splitting this distribution for different values of diameter, until a good match with the experimental film footprint was found. This process resulted in the choice of a diameter corresponding to the 3rd quartile of the cumulative volumetric distribution. An equivalent splitting was done in terms of the masses associated with each injector. For the surface film model, thermo-capillary and contact angle forces were considered, while no stripping model was utilised, since the film would not reach conditions were stripping can occur until a very high number of injections. Due to the lack of experimental data for urea, the contact angle for water was used for this case. Heat flux from both the fluid and the solid was considered, as well as the phase change, with a limitation on the minimum film height before both models activate. This is necessary to ensure the stability of the numerical solution when the mass of the liquid layer is very small.

One of the most important parameters regarding spray cooling is the mass flux of the spray [29]. To ensure that the simulations are carried in conditions similar to the experimental ones, a comparison between the film footprint obtained numerically and the experimental one is performed. The experimental data were extracted from a video recording of the top of the plate, showing the formation and evolution of the film on the plate target. For this case, a different set of conditions were considered, with the same mass flow rate (100 kg/h) but with a lower gas temperature (300° C) to allow film formation already from the first injection. A suitable frame was then selected after the end of the first injection, and the two main dimensions of the film footprint were evaluated. The conversion from pixels to meters was performed using as reference the window dimension and extracting the pixel to meters conversion ratio from this data. The error associated with this method was evaluated to be around 1%. A visual comparison of the two different footprints can be seen in Figure 7, where the two halves of the experimental and numerical film are put together side by side. While the comparison in terms of overall film area shows a good agreement, the global shape of the film could not be captured, with the maximum error being on the longitudinal extension, with a length of 28.78 mm measured from the optical measurements,
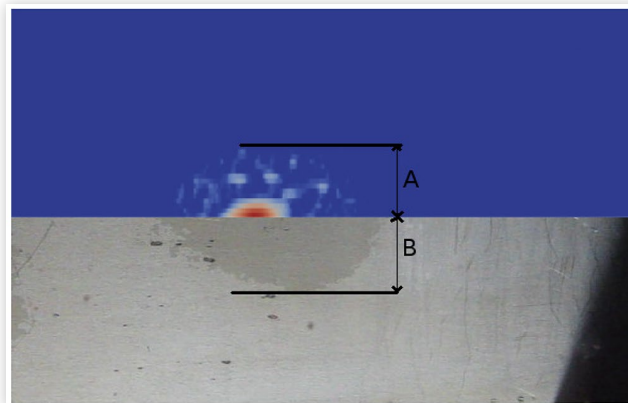
against an estimated length of 18.12 mm. This large error in the cross flow direction can be attributed to a higher number of small diameter parcels with respect to the experimental spray, which will lead to a considerable portion of the spray being dragged away from the target plate, thus leading to a smaller film footprint in the cross flow direction (see Figure 8). While the area of the film formed is similar, the shape of the footprint appears to be quite different, in particular the upstream section, which shows a reduction of the width of the footprint that is not reproduced numerically. This discrepancy can be attributed to a different diameter distribution with respect to the one used in the calculations, which appears to be more populated by smaller diameters with respect to the real spray distribution. This is due to the technique used for the evaluation of the spray diameters, as PDA is not capable to capture the large blobs that form during the initial and final phase of the low-pressure injection [30].

After this simulation, the same spray setup was utilised in the high temperature conditions. In this case, very little film formation is expected in the first injection for the downstream hole, while film formation around the impingement area will be more and more evident for subsequent injections. In the Figure 9 two frames extracted from the simulation at the end of the first and second injection are shown, with both the film height and solid temperature shown side to side. It is apparent that the different conditions between the two upstream holes and the downstream one, and in particular

FIGURE 8 Visualization of the spray for the downstream nozzle. The parcels colors refer to the diameter.
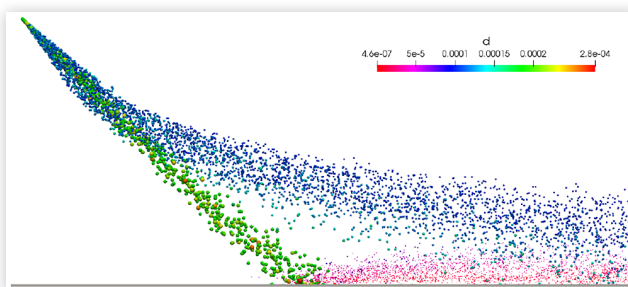
FIGURE 9 Side to side comparison of the film height and the solid temperature obtained from simulations for the first (a) and second (b) injections. Film height is in m and temperature is in K.

(a)

(b)
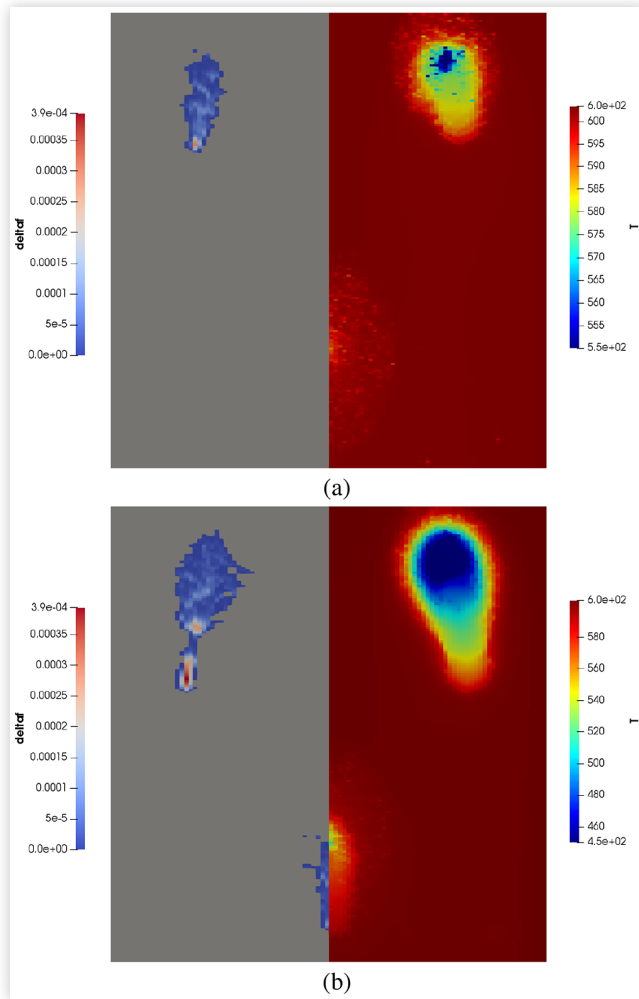
the different mass fluxes produce different results in term of spray cooling, leading to film formation for the two upstream holes and no film formation until the second injection for the downstream hole. This situation is compounded by the different impingement angle that will lead to different K numbers for the two holes, thus producing different impingement regimes for the parcels, influencing the heat flux between the spray and solid region. This strong interaction between spray and film also pushes the newly formed film along the direction of the plate, generating an elongated thermal footprint. The higher momentum associated with the thicker parts of the film produce the longer trails that can be seen for the upstream hole with respect to the downstream one. This effect more than compensates the reduced tangential momentum transfer between spray and film for these two holes with respect to the downstream one, where the low thickness of the film means that the viscous forces due to the interaction with the wall prevail on the momentum transfer from the spray and the surrounding gas. Between injections evaporation reduces the thickness of the film, meaning that the film motion is univocally associated with the injection phase.

This ceases to be true for a high number of injections, where the reduction in heat flux from the wall indicates that the film does not evaporate enough between injections and the shear stresses between film and gases are able to transport it downstream. In Figure 10 the experimental and numerical footprint are compared, showing the aforementioned effect, with the numerical footprints showing an excess of film transport with respect to the experimental ones. This difference in transport can be also attributed to the uncertainty about urea properties. In this work, to overcome the lack of detailed data about urea, the authors used the same function for water, leading to low viscosities even for temperatures below the urea solidification temperature. As an example of the effect of the film transport in later injections, a frame from the end of the sixth injection is also included (see Figure 11), to show that the same thermal trace associated with film transport can be found for later injections in the experimental case.

FIGURE 10 Experimental (left) and numerical (right) temperature fields side by side: at the end of the first (a), second (b), and third (c) injections.

(a)

(b)

(c)
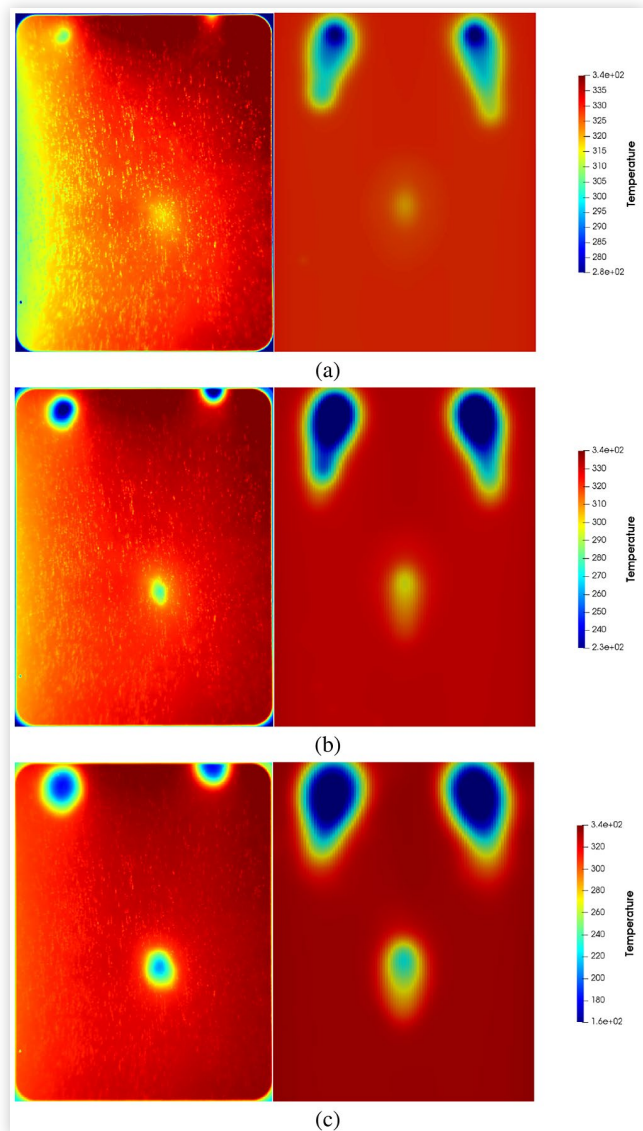
FIGURE 11 Termography at the end of the sixth injection. The effects of film transport are evident.

FIGURE 12 Back plate temperature: comparison between numerical and experimental averaged values.
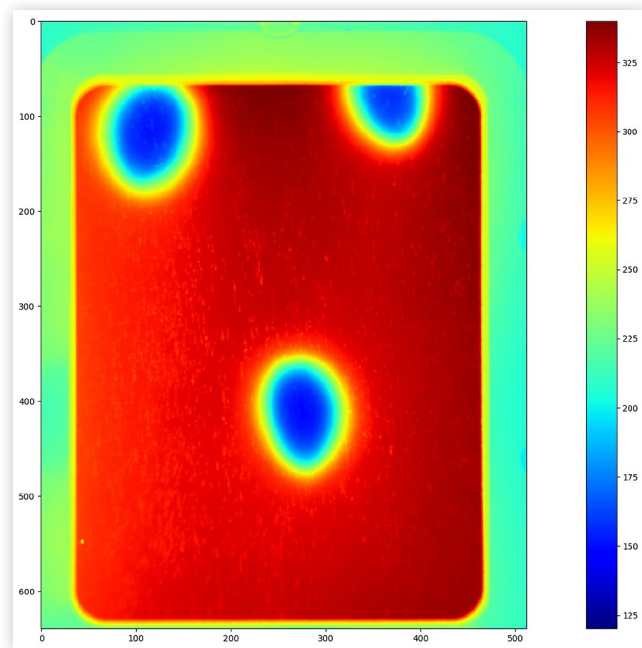

Figure 10 also highlights some of the difficulties associated with the simulation of this particular case. First of all, a temperature gradient can be seen across the transversal section of the plate. This is associated with the presence of a window on the left side of the tunnel, used to provide access for Phase Doppler Anemometry. The effects of the radiative heat exchange on the temperature can be quite important, in particular for the downstream hole for lower injected masses, as the temperature difference between the hotter and colder side of the plate can be in the same range as the temperature drop associated with the spray cooling. Another important discrepancy between the numerical and experimental cases is associated with the misalignment of the injector with respect to the axis of the test bench. From a CFD point of view the positions of the holes is perfectly symmetric, whereas at the experimental level the mounting of the injector cannot be this precise and the final result can be a slightly skewed spray with respect to the channel axis. This misalignment will lead to different areal mass fluxes for the three holes, with a stronger effect for the two upstream holes, where the right hole will have a higher mass flux than the left one. Since the misalignment mostly affects the upstream impingement cones (the side cones), that were not the focus of this analysis, it was decided not to reproduce this in the simulations, aligning the spray with the flow instead. For this reason the thermal analysis was focused on the downstream hole, as this hole was the one less affected by the uncertainties linked to the spray misalignment and to the radiative heat transfer. The reference values used for this comparison are obtained from an averaging of the temperature around the center of the thermal footprint, using a round kernel of 2.24 mm of diameter. To reproduce this averaging, the data from the simulation were post processed in Paraview, extracting a cut around the impingement footprint of the downstream nozzle with the
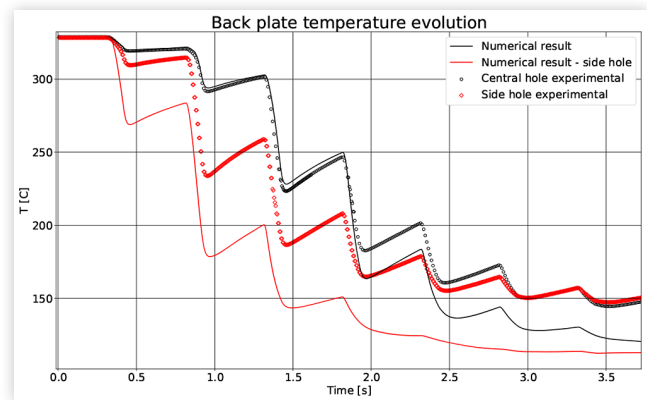
same diameter as the averaging kernel, and then performing area averaging on the selected cut. The comparison between experimental and numerical data is shown in Figure 12, showing that the model has a good agreement with experimental data, capturing the transition between the different boiling regimes. A higher temperature drop can be seen in the fourth injection, probably due to an over estimation of the critical heat flux temperature. In the graph the temperature drop for the upstream left hole is also reported. The left hole was chosen for this analysis as the right hole was not completely in frame in the experimental thermography. As the temperature drop for this hole is stronger than for the downstream one, it can be used to evaluate the performance of the model at lower plate temperatures, where as it can be seen, the model reproduces the reduction in heat flux associated with the transition from the nucleate boiling to pure conduction. In particular, the third and fourth numerical injection have temperature drops comparable with the ones for the fourth and fifth experimental injections.

The transition between the different evaporation regimes is more evident when looking at the graph of the temperature gradient as function of the plate temperature (see Fig. 13). As during the first injection almost no film is formed, the results confirm that for temperatures higher than the Leidenfrost temperature a very strong limit in term of heat flux between

FIGURE 13 Temperature gradient as a function of the wall Temperature. The empty dots represent experimental data, while the crosses refer to numerical ones.
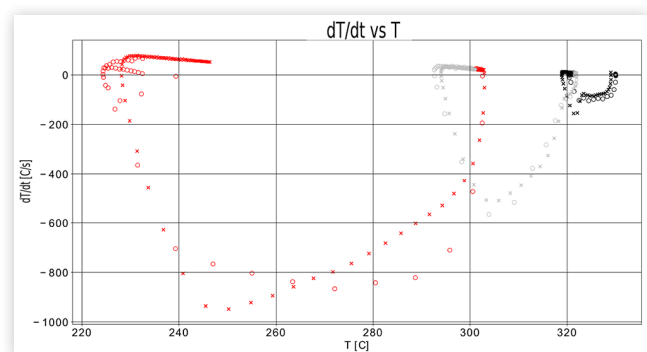
solid and spray exists. In fact, for this injection the tempera-ture gradient shows a clear plateau, that cannot be found for the following injections. The higher temperature drops for the upstream cones that can be found both experimentally and numerically must be therefore linked to the different mass fluxes and interaction regime associated with the upstream holes. From this analysis, is apparent that interaction in this regime will not produce a noticeable thermal load for compo-nents of the after-treatment system, while producing a benefi-cial effect in term of spray atomisation. This is due to the fact that spray interaction at such temperatures will result in thermal breakup of the parcels, increasing the effective heat transfer area of the spray and thus improving the atomisation and evaporation of urea and its conversion into ammonia. The transition from the first injection, that happens in the Leidenfrost regime, to the nucleate boiling regime is evident when looking at the next injections (marked with different colors in the graph). The second injection starts from a temperature slightly higher than the Leidenfrost temperature, then drops below this limit and shows a quick increase in the temperature gradient associated with the transition boiling regime. These temperature ranges can be dangerous in term of solid deposit formation, because of the high heat transfer coefficient involved in this phase change regime, that can quickly reduce the temperature of the components of the ATS and lead to the formation of a persisting liquid film, which is the main reason for solid deposit formation [31]. These large heat transfer coefficients can also be exploited to ensure quick evaporation of the film, if the heat subtracted by the evapora-tion can be quickly replenished between injections, with a hot gas EGR or a thermal resistor. In the third injection instead the transition to the nucleate boiling regimes is apparent, as the critical heat flux temperature is crossed. Experimentally this point coincides with the maximum thermal gradient, while for our model the maximum gradient appears in the next injection, together with the maximum temperature drop. This can be due to a mismatch between the evaluated average droplet saturation temperature, that leads to a wrong estima-tion of the critical heat flux excess temperature. As in these conditions the saturation temperature of the droplet is only a function of the species concentrations (as there are no large pressure gradients in the system), this mismatch can be accounted for considering the uncertainties in the model for the urea saturation pressure. In Figure 12 it can be seen that as the temperature of the impingement area of the upstream hole crosses this temperature (by the end of the second injection), the temperature reduction for subsequent injections drop below the previous ones. As the solid tempera-ture is influenced primarily from the heat flux to the spray, and the low temperature regions in the impingement area are also the areas where film formation occurs at first, it is apparent that the spray modeling is of paramount importance when evaluating the thermal behaviour of components of the ATS. The uncertainties in the spray model, and in particular the diameter distribution used to represent the real spray can therefore lead to large variations in the heat fluxes evaluated numerically with respect to the experimental ones. This is due to the fact that differences in the entrained mass will lead to different mass fluxes in the impingement area, affecting directly the heat flux to the wall. This mismatch in the

FIGURE 14 Temperature gradient as a function of the wall Temperature, with only numerical data. The arrows indicate the time direction.
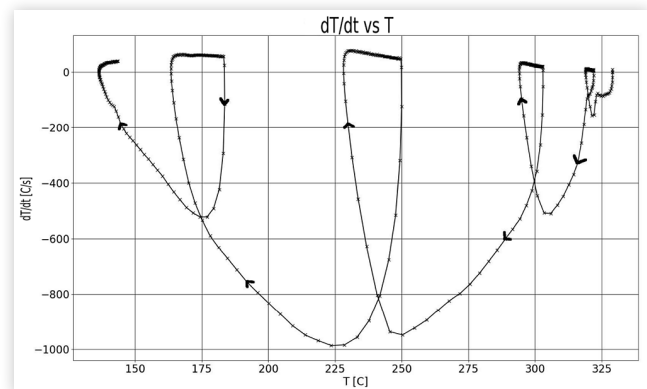
evaluation of the critical heat flux temperature can be seen more clearly when including the fourth injection in the temperature/temperature gradient graph. In Figure 14 the maximum temperature gradient corresponds to a back plate temperature of 225 C, with a difference of 40 degrees with respect to the experimental value.

Conclusions

In this work a comprehensive methodology capable of capturing the effects of the thermal interaction between spray, film and wall has been developed and applied to an experi-mental test case from Empa. The heat transfer model devel-oped extends the previously developed Kuhnke model [19] that was integrated inside the OpenFOAM library, integrating a limitation of the heat flux between spray and wall, depending on the boiling regime, as described by the Nukiyama curve. The model was developed starting from the data received from EMPA, that allowed the authors to evaluate the temperature ranges for the different evaporation regimes. In the selected case, a three-hole injector is used to inject UWS on a thin metal plate suspended in a tunnel with a square cross section. The temperature of the plate was measured with infrared ther-mometry on the back side of the plate. To compare in a mean-ingful way numerical and experimental temperature, at first a calibration of the spray model was performed using video data from an experiment at low temperature. This allowed a direct evaluation of the area of the film formed at the end of the injection, that directly affects the mass flux of the spray, and thus the heat exchange due to spray cooling. The spray model used allowed the authors to achieve comparable dimen-sions of the film footprint between the experimental and numerical cases, with a mismatch in the overall shape of the footprint due to a discrepancy in the spray diameter distribu-tion between the real and numerical case, where the numerical distribution seems to be centered towards smaller diameters than the real case. The same setup was used to simulate the high temperature case. First of all, the overall shape of the calculated thermal footprint reveals a good agreement with experimental data, where the strongest difference between the

two cases is due to a higher transport of the film in the case of the numerical simulations. This emphasizes the importance of using reliable data to determine UWS viscosity as well as surface tension and contact angle. The evolution of the chemical composition of UWS also plays an important role since it affects the overall kinematic and thermal behaviour of the film. The evaluation of the temperature in the center of the footprint of the downstream hole reveals that the model can capture the transition in boiling regimes. However, the combination of several uncertainties coming from both the experiments and the numerical models makes the prediction of the thermal footprint a challenging task. In particular, the approximations introduced to model the low-pressure injection and the consequent propagation of the spray inside of the gas stream leads to an evaluation of the spray mass flux at the wall that may differ from the experimental one. This flux is the driving parameter of the spray cooling effect. In any case, the results of the calculations show that, apart from some discrepancies in capturing the transition in boiling regimes, the macroscopic effects of spray wall interaction could be captured: Leidenfrost regime with thermal breakup and transition from dry to wet wall interaction with generation of liquid film layer. Based on these considerations, the authors can state that the actual model can be adopted to have a realistic estimation of the risk of solid deposits formation in the dosing unit for SCR systems.

References

1. Johnson, T., "Review of Vehicular Emissions Trends," *SAE Int. J. Engines* 8, no. 3 (2015): 1152-1167.

2. Koebel, M., "Thermal and Hydrolytic Decomposition of Urea for Automotive Selective Catalytic Reduction Systems: Thermochemical and Practical Aspects," *Industrial and Engineering Chemistry Research - IND ENG CHEM RES* 42 (2003): 04.

3. Tian, X., Xiao, Y., Zhou, P., Zhang, W. et al., "Study on the Mixing Performance of Static Mixers in Selective Catalytic Reduction (SCR) Systems," *Journal of Marine Engineering & Technology* 14, no. 2 (2015): 57-60.

4. Liao, Y., Dimopoulos Eggenschwiler, P., Furrer, R., Wang, M. et al., "Heat Transfer Characteristics of Urea-Water Spray Impingement on Hot Surfaces," *International Journal of Heat and Mass Transfer* 117 (2017): 10.

5. Brack, W., Heine, B., Birkhold, F., Kruse, M. et al., "Kinetic Modeling of Urea Decomposition Based on Systematic Thermogravimetric Analyses of Urea and Its Most Important By-Products," *Chemical Engineering Science* 106 (2014): 1-8.

6. Smith, H., Lauer, T., Mayer, M., and Pierson, S., "Optical and Numerical Investigations on the Mechanisms of Deposit Formation in SCR Systems," *SAE International Journal of Fuels and Lubricants* 7 (2014): 525-542.

7. Birkhold, F., Meingast, U., Wassermann, P., and Deutschmann, O., "Analysis of the Injection of Urea-Water-Solution for Automotive SCR Denox-Systems: Modeling of Two-Phase Flow and Spray/Wall-Interaction," *Analysis* 1 (2006): 01.

8. Stradella, L. and Argentero, M., "A Study of the Thermal Decomposition of Urea, of Related Compounds and Thiourea Using dsc and tg-ega," *Thermochimica Acta* 219 (1993): 315-323.

9. Eichelbaum, M., Siemer, A.B., Farrauto, R.J., and Castaldi, M.J., "The Impact of Urea on the Performance of Metal-Exchanged Zeolites for the Selective Catalytic Reduction of Nox—Part II. Catalytic, ftir, and Nmr Studies," *Applied Catalysis B: Environmental* 97, no. 1 (2010): 98-107.

10. Koebel, M., Elsener, M., and Kleemann, M., "Urea-SCR: A Promising Technique to Reduce Nox Emissions from Automotive Diesel Engines," *Catalysis Today* 59, no. 3 (2000): 335-345.

11. Stein, M., Bykov, V., Bertótiné Abai, A., Janzer, C. et al., "A Reduced Model for the Evaporation and Decomposition of Urea-Water Solution Droplets," *International Journal of Heat and Fluid Flow* 70 (2018): 216-225.

12. Birkhold, F., Meingast, U., Wassermann, P., and Deutschmann, O., "Modeling and Simulation of the Injection of Urea-Water-Solution for Automotive SCR Denox-Systems," *Applied Catalysis B: Environmental* 70 (2007): 119-127.

13. Wruck, N., *Transientes Sieden von Tropfen beim Wandaufprall* (Shaker, 1998)

14. Gradeck, M., Seiler, N., Ruyer, P., and Maillet, D., "Heat Transfer for Leidenfrost Drops Bouncing Onto a Hot Surface," *Experimental Thermal and Fluid Science* 47 (2013): 14-25.

15. Bai, C. and Gosman, A., "Development of Methodology for Spray Impingement Simulation," SAE Technical Paper 950283 (1995). https://doi.org/10.4271/950283.

16. Bai, C., Rusche, H., and Gosman, A., "Modeling of Gasoline Spray Impingement," *Atomization and Sprays - Atomization Sprays* 12 (2002): 1-28.

17. Smith, H., Zöchbauer, M., and Lauer, T., "Advanced Spray Impingement Modelling for an Improved Prediction Accuracy of the Ammonia Homogenisation in SCR Systems," SAE Technical Paper 2015-01-1054 (2015). https://doi.org/10.4271/2015-01-1054.

18. Kuhnke, D., *Spray/Wall Interaction Modelling by Dimensionless Data Analysis* (Shaker, 2004)

19. Nappi, A., Montenegro, G., Onorati, A., and Della Torre, A., "A Cht Framework for the Cfd Analysis of the Spray-Wall Thermal Interaction in the Dosing Unit of SCR Systems for Diesel Engines," *AIP Conference Proceedings* 2191 (2019): 020118.

20. Mundo, C., Sommerfeld, M., and Tropea, C., "Droplet-Wall Collisions: Experimental Studies of the Deformation and Breakup Process," *International Journal of Multiphase Flow* 940525 (1995): 151-173.

21. Nagaoka, M., Kawazoe, H., and Nomura, N., "Modeling Fuel Spray Impingement on a Hot Wall for Gasoline Engines," SAE Technical Paper 940525 (1994). https://doi.org/10.4271/940525.

22. Wachters, L. and Westerling, N., "The Heat Transfer from a Hot Wall to Impinging Water Drops in the Spheroidal State," *Chemical Engineering Science* 21, no. 11 (1966): 1047-1056.

23. Fujio Akao, S.M., Araki, K., and Moriyama, A., "Deformation Behaviours of a Liquid Droplet Impinging Onto Hot Metal Surface," *Trans. Iron Steel Inst. Jpn.* 20 (1980): 737-743.

24. Foucart, H., Habchi, C., Le-coz, J.-F., and Baritaud, T., "Development of a Three Dimensional Model of Wall Fuel Liquid Film for Internal Combustion Engines," *SAE International Journal of Engines* 107, 02 (1998): 16.

25. Incropera, F.P. and Witt, D.P.D., *Fundamentals of Heat and Mass Transfer* (Wiley and Sons, 2007)

26. Zuber, N., "On the Stability of Boiling Heat Transfer," *Trans. Am. Soc. Mech. Engrs.* 80 (1958): 4.

27. Liao, Y., Dimopoulos Eggenschwiler, P., Spiteri, A., Nocivelli, L. et al., "Fluid Dynamic Comparison of Adblue Injectors for SCR Applications," *SAE International Journal of Engines* 8 (2015): 09.

28. Nocivelli, L., Montenegro, G., Onorati, A., Curto, F. et al., "Quantitative Analysis of Low Pressure-Driven Spray Mass Distribution and Liquid Entrainment for SCR Application through a Mechanical Patternator," SAE Technical Paper 2017-01-0965 (2017). https://doi.org/10.4271/2017-01-0965.

29. Ciofalo, M., Piazza, I.D., and Brucato, V., "Investigation of the Cooling of Hot Walls by Liquid Water Sprays," *International Journal of Heat and Mass Transfer* 42, no. 7 (1999): 1157-1175.

30. Bracho, G., Postrioti, L., Moreno, A., and Brizi, G., "Experimental Study of the Droplet Characteristics of a SCR Injector Spray Through Optical Techniques," *International Journal of Multiphase Flow* 135 (2021): 103531.

31. Budziankou, U., Quissek, M., and Lauer, T., "A Fast Modeling Approach for the Numerical Prediction of Urea Deposit Formation," *SAE International Journal of Advances and Current Practices in Mobility* 2 (apr 2020): 1337-1355.

Contact Information

Antonello Nappi, Ph.D.
antonello.nappi@Polimi.it

Definitions, Acronyms, Abbreviations

ATS - After Treatment System

BC - Boundary Conditions

CFD - Computational Fluid Dynamics

CHF - Critical Heat Flux

CHT - Conjugate Heat Transfer

RANS - Reynolds-averaged Navier-Stokes

UWS - Urea Water Solution